Point Cloud Synthesis Using Inner Product Transforms

Ernst Röell [1 2]   **Bastian Rieck** [1 2 3]

Abstract

Point-cloud synthesis, i.e. the generation of novel point clouds from an input distribution, remains a challenging task, for which numerous complex machine-learning models have been devised. We develop a novel method that encodes geometrical-topological characteristics of point clouds using inner products, leading to a highly-efficient point cloud representation with provable expressivity properties. Integrated into deep learning models, our encoding exhibits high quality in typical tasks like reconstruction, generation, and interpolation, with inference times orders of magnitude faster than existing methods.

1. Introduction

Point clouds are a data modality of crucial relevance for numerous applications. While computer graphics is the predominant application area, where point clouds are often used as precursor to more structured representations like meshes, they also occur in higher dimensions in the form of sensor data, for instance. However, the synthesis of hitherto-unseen point clouds from a given distribution still proves to be a challenging task, with numerous models aiming to address it (Xu et al., 2023). The complexity arises largely because of the sparsity and 'set-like' structure of point clouds, making it hard to generalise existing machine-learning architectures directly. State-of-the-art methods thus typically require large amounts of compute, exhibiting long training and inference times. With recent work (Tancik et al., 2020) demonstrating that a change of perspective—like the switch from raw coordinates to Fourier-based features—can make comparatively simple deep-learning architectures competitive in computer-vision tasks, our paper explores the question to what extent novel representations of point clouds can lead to gains in computational performance *without* sacrificing quality.

To obtain such a novel representation, we use a multi-scale geometrical-topological descriptor (Turner et al., 2014) based on *inner products* of coordinates representing a high-dimensional shape. With suitable approximations, which we present in this paper, this descriptor permits us to represent a point cloud as a *single* 2D image. Unlike other single-view representations, however, the coordinates of the image represent a different 'domain,' namely geometrical-topological aspects of a point cloud. In fact, this mapping is computationally efficient and *injective*, making it in theory possible to reconstruct a point cloud from its descriptor. We refer to this mapping as the *Inner Product Transform* (IPT) and use it for the generation of point clouds.[1]

Our paper is built on two core notions, the first one being that we treat point-cloud generation as a two-step task, with the first step being an image-generation task, yielding a two-dimensional descriptor, followed by a (multi-modal) image-to-point-cloud *reconstruction* task. We realise the two steps using separate machine-learning models, thus substantially decreasing architectural complexity—in effect, we represent a point cloud as a special image that can be *generated*, providing a bridge to the point-cloud domain. The second core notion is that the generated image is a faithful, i.e. *injective*, representation of the point cloud, indicating that it is possible to perfectly reconstruct a point cloud from its descriptor. Our paper makes the following **contributions**:

1. We present a novel model based on inner products for generating point clouds whose quality exceeds or is on a par with other state-of-the-art methods—while exhibiting training and inference times that are *orders of magnitude faster*.
2. We show that our representation yields a stable latent space, which permits (i) high-quality interpolation tasks, and (ii) solving different out-of-distribution tasks *without* the need for retraining while still maintaining high quality.
3. We prove injectivity and other advantageous properties of our descriptor, allowing the generalisation of our method to point-clouds of arbitrary dimensions.

---

[1]Helmholtz Munich, Munich, Germany [2]Technical University of Munich, Munich, Germany [3]University of Fribourg, Fribourg, Switzerland. Correspondence to: Bastian Rieck <bastian.grossenbacher@unifr.ch>.

---

[1]For readers familiar with computational topology, the IPT is a special case of the *Euler Characteristic Transform* (ECT). Our focus on point clouds permits us to formulate the IPT without any background knowledge in computational topology, while also resulting in substantially simplified proofs.

2. Related Work

Point clouds being a nigh-ubiquitous data modality, numerous models already exist to tackle classification or generation tasks (Xu et al., 2023). The lack of structure, as well as the requirement of permutation invariance, imposes constraints on the underlying computational architecture, typically substantially increasing model complexity (Qi et al., 2017; Zaheer et al., 2017). To solve generation tasks, many methods opt for *jointly* learning the generation of the shape, i.e. the surface or object the points are sampled from, as well the mapping of points onto that object. This core idea drives several recent state-of-the-art models, including Point-Voxel CNN (Liu et al., 2019), PointFlow (Yang et al., 2019), Soft-Flow (Kim et al., 2020), Point Voxel Diffusion (Zhou et al., 2021, PVD) and LION (Zeng et al., 2022)). While these models exhibit high-quality results, their architectures require long training and inference times.

By contrast, our approach only needs to model a distribution of geometrical-topological descriptors, represented as 2D images, from which we subsequently *reconstruct* a point cloud again. While reconstructing point clouds from images is an active field of research (see Fahim et al. (2021) for a survey on single-view reconstruction), such images are typically depth images or snapshots taken from a specific position around the object. As such, they are not necessarily yielding a faithful, unique representation of an object.

A crucial property of our method (IPT) is that it yields a faithful representation, hence permitting an injective mapping between the image domain and the shapes we aim to reconstruct (or generate). This is due to the fact that the IPT is a special case of a general geometrical-topological descriptor, the *Euler Characteristic Transform* (ECT), which studies shapes at multiple scales and from multiple directions, yielding a unique characterisation of a shape (Turner et al., 2014). Being a stable (Dłotko, 2024) and efficient descriptor, the ECT is often used to solve questions in data science, mostly in the form of 'hand-crafted' features for classification and regression tasks (Amézquita et al., 2021; Crawford et al., 2020; Marsh et al., 2024; Munch, 2023; Nadimpalli et al., 2023). Recent work addressed this shortcoming and enabled the use of the ECT in machine-learning applications in the form of a generic differentiable computational layer (Röell & Rieck, 2024). Notably, the ECT remains a unique characterisation even when using a finite number of directions (Curry et al., 2022; Ghrist et al., 2018), meaning that, theoretically, it can inverted to reconstruct the input data. Practically, inversion is presently possible only for select data modalities like planar graphs (Fasy et al., 2018). While restricted to point clouds, our method is the first to enable the inversion of such a descriptor for input data of arbitrary dimensionality, making it possible to use it in the context of a generative model.

3. Methods

Our method, the *Inner Product Transform* (IPT), can be intuitively understood as a filtering process of point clouds, employing different sets of hyperplanes, created by a set of *directions* (i.e. normal vectors). The inner products of point cloud coordinates with a direction vector are then used to parametrise a *curve* that counts the number of points below the hyperplane. By stacking curves, we obtain a 2D image representation of the point cloud. The IPT is a special case of the *Euler Characteristic Transform* (Turner et al., 2014, ECT), but our subsequent description is self-contained, does not require any knowledge of topology, and presents simplified proofs of all properties.

3.1. Inner Product Transforms

Let S^{n-1} denote the unit sphere in $\mathbb{R}^n$. Given a point cloud $X \subset \mathbb{R}^n$, a fixed direction vector $\xi \in S^{n-1}$ and a *height* $h \in \mathbb{R}$, we define the set $X_{\xi,h} := \{x \in X \mid \langle x, \xi \rangle \leq h\}$, where $\langle x, \xi \rangle$ denotes the standard Euclidean dot product. The set $X_{\xi,h}$ is the set of points below the hyperplane spanned by $\langle x, \xi \rangle = h$, and we denote its cardinality by $\chi(X_{\xi,h})$.[2] We then define the *Inner Product Transform* as the function

$$
\begin{aligned}
\mathrm{IPT}(X) \colon S^{n-1} \times \mathbb{R} &\to \mathbb{N} \\
(\xi, h) &\mapsto \chi(X_{\xi,h}).
\end{aligned} \tag{1}
$$

A point $x \in X$ is included in $X_{h,\xi}$, thus affecting $\chi(X_{\xi,h})$, if and only if its height $h_x := \langle x, \xi \rangle$ along ξ is less than h. We can thus formulate the contribution of a point x to the IPT along each direction in terms of an *indicator function*:

$$
\mathbb{1}_x(\xi, h) := \begin{cases} 1 & \text{if } \langle \xi, x \rangle \leq h \\ 0 & \text{otherwise} \end{cases} \tag{2}
$$

This enables us to rewrite Eq. (1) as

$$
\begin{aligned}
\mathrm{IPT}(X) \colon S^{n-1} \times \mathbb{R} &\to \mathbb{N} \\
(\xi, h) &\mapsto \sum_{x \in X} \mathbb{1}_x(\xi, h).
\end{aligned} \tag{3}
$$

Following ideas from Röell & Rieck (2024), we can replace all indicator functions with sigmoid functions, i.e.

$$
\begin{aligned}
\widehat{\mathrm{IPT}}(X) \colon S^{n-1} \times \mathbb{R} &\to \mathbb{R} \\
(\xi, h) &\mapsto \sum_{x \in X} S(\lambda(\langle \xi, x \rangle - h)),
\end{aligned} \tag{4}
$$

where λ denotes a scale parameter, which controls how closely the sigmoid function approximates the indicator function (Appendix C describes stability experiments). In practice, we sample n_d directions and discretise all heights with n_h steps, thus turning $\widehat{\mathrm{IPT}}$ into an *image* of resolution $n_h \times n_d$.

---

[2]For readers familiar with topology, this notation is an allusion to the *Euler Characteristic*.
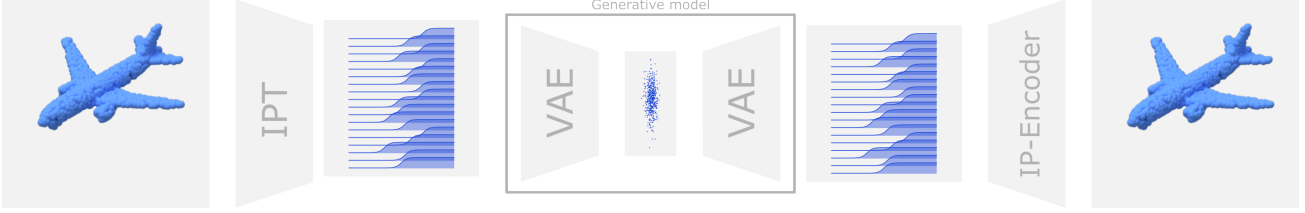
Figure 1: Given a point cloud on the left, we compute its *Inner Product Transform* (IPT), which results in a compressed representation. For generative tasks, we train a generative model (middle) to reconstruct and generate the distribution of IPTs. The (possibly-generated) IPT is then passed through the encoder model to obtain the reconstructed (or novel) point cloud. Our pipeline is decoupled, permitting *any* generative image model to be used to generate point clouds. Further image compression can be employed to obtain a highly-compact representation of the input data.

Properties. The IPT and its approximation from Eq. (4) satisfy several important properties. We first note that the IPT is *injective*, i.e. a point cloud can be perfectly reconstructed from its descriptor.

Theorem 1. *The IPT is* injective*, i.e. $X \neq Y$ implies that* $\mathrm{IPT}(X) \neq \mathrm{IPT}(Y)$ *for two point clouds X, Y.*

While this is a known result (Ghrist et al., 2018; Turner et al., 2014), we provide a new, accessible proof using elementary theory. An important consequence of injectivity is that it allows us to formulate a metric for the set of point clouds contained in a ball of fixed radius.

Lemma 1. *Let $B_n(R)$ denote a ball of radius R in $\mathbb{R}^n$. For two point clouds $X, Y \in B_n(R)$, define their* distance *as*

$$d(X, Y) := \frac{1}{|\Xi|} \sum_{\xi \in \Xi} \|\mathrm{IPT}(X)_{\restriction \xi} - \mathrm{IPT}(Y)_{\restriction \xi}\|_2, \quad (5)$$

where Ξ is a finite set of directions and $\| \cdot \|_2$ is the L^2-norm restricted to the interval $[-R, R]$. The function $d(\cdot, \cdot)$ satisfies the definition of a metric.

When approximating the IPT via Eq. (4) and a finite number of directions in practice, the metric defined in Lemma 1 corresponds to the pixel-wise mean squared error between discretised IPTs. Hence, given sufficient directions, we can formulate a *loss function* based on this metric, which admits a highly-efficient implementation and will turn out to lead to high-quality results. We also obtain a result that permits us to calculate IPTs from disjoint unions of point clouds.

Lemma 2. *Let $X, Y \subset \mathbb{R}^n$ be disjoint point clouds, then*

$$\mathrm{IPT}(X \cup Y) = \mathrm{IPT}(X) + \mathrm{IPT}(Y). \quad (6)$$

Finally, we can prove that the IPT is *surjective* on convex linear combinations.

Theorem 2. *Given two point clouds $X, Y \subset \mathbb{R}^n$. The IPT is* surjective *for the rational linear subspace spanned by* $\mathrm{IPT}(X)$ *and* $\mathrm{IPT}(Y)$*, up to a rational scaling factor. In*

particular, for $p, q \in \mathbb{N}_0$ with $0 \leq p \leq q$ we have

$$\frac{p}{q}\mathrm{IPT}(X) + \frac{q-p}{q}\mathrm{IPT}(Y) = \frac{1}{q}\mathrm{IPT}(Z), \quad (7)$$

where $Z = \cup_p X \cup_{q-p} Y$.

This theorem provides an interpretation of the interpolation between two IPTs in terms of the input point clouds. A direct consequence of Theorem 2 is that, along the *linear interpolation* between two IPTs, there are only valid IPTs, i.e. each interpolation step affords a perfect reconstruction in theory. We analyse this aspect further in Section 4.5.

3.2. The IP-Encoder

The existence of Theorem 1 unfortunately does not lead to a practical algorithm for 'inverting' an IPT. We therefore suggest an approach based on neural networks and describe the IP-Encoder, which encodes an IPT to a point cloud. Subsequently, this will enable us to learn *distributions* of IPTs and reconstruct new point clouds in a generative setting and, as we shall see, even in the setting of out-of-distribution data. Since our representation is permutation-invariant, our IP-Encoder model directly inherits this invariance, which substantially reduces the complexity of its architecture.

Model architecture. Given the structure of the IPT as an image, a standard CNN architecture would suggest itself. However, since the direction vectors $\xi \in S^{n-1}$ cannot be consistently ordered along one dimension, we need to reframe the input data. Specifically, we consider an IPT, normalised to $[-1, 1]$, as a *multi-channel, one-dimensional signal*. Our IP-Encoder model then consists of four 1D convolutional layers followed by three fully-connected layers. While this architecture is conceptually simple, the set of directions is only implicitly encoded through a fixture in the channels in the neural network. To *generate* a novel IPT, we can use any generative model for images. In our experiments, we will use an architecture based on a convolutional variational autoencoder, denoted by IP-VAE. Please refer to Appendix E for more details.

Topological point cloud optimisation. As an alternative to the machine-learning model above, we also investigate whether the inversion of an IPT can be turned into an *optimisation problem*. Due to the differentiability of our approximation $\widehat{\text{IPT}}$ and given a known IPT,[3] minimising a loss function, such as the one described in Lemma 1, using backpropagation should result in a suitable approximation of the unknown point cloud one wishes to recover. However, while this works in *theory*, it requires the input and target to be a correct IPT of a point cloud. In practice, this is not guaranteed: Generative models may sample from their latent spaces and output samples that are *close* to being an IPT of a point cloud without actually satisfying all structural constraints. To some extent, we argue that this is even the desired behaviour since a generative model would otherwise just rehash its inputs. Hence, any optimisation-based method will not necessarily result in realistic reconstructions in a generative setting. We nevertheless investigate an optimisation procedure in an ablation study in the appendix and refer readers to Figure C.3 therein.

Topological loss functions. The fact that Lemma 1 shows the IPT to be a metric naturally poses the question if it can be used as an effective and efficient loss term, to which we provide an affirmative answer. While in principle the IPT is sufficient as a loss term for training a point cloud reconstruction model, training time can be reduced through a combination of a low-resolution (64×64) IPT combined with the Chamfer Distance (CD). The CD is a fast-to-compute (pseudo-)metric often used in point cloud evaluation (see Appendix D for more details). The IPT loss ensures that the overall geometry and point cloud density of the object is captured, whereas the CD loss ensures that fine-grained details are accounted for. Building a joint loss, combining the IPT and CD, thus results in a density-aware loss term that takes the global density of a point cloud into account.

Latent space. Interpolation between samples provides valuable insight into the capacities of generative models. Using Theorem 2, we can provide an intuition for interpolation using IPTs. To this end, suppose we perform linear interpolation between point clouds X, Y, using a parameter p over the interval $[0, 1]$, which is partitioned in q equidistant steps. Theorem 2 states that at step p/q, the point cloud $Z = \cup_p X \cup_{q-p} Y$ is the union of p copies of X and $q - p$ copies of Y. During the interpolation, the number of copies of X is increased and the number of copies of Y is reduced. We may interpret this intuitively as transporting 'mass' from Y to X over the course of q steps. Our IP-Encoder model averages all copies during reconstruction in a natural fashion, resulting in smooth transitions between point clouds.

---

[3]We will drop the approximation notation whenever we are dealing with computational experiments to simplify the flow.

4. Experiments

We demonstrate the effectiveness, efficiency, and overall utility of our IP-Encoder through a comprehensive suite of experiments. Among other things, we show that our IP-Encoder model can (i) effectively reconstruct shapes, (ii) create novel point clouds from *generated* IPTs, and (iii) effectively compress and upsample point clouds. All our experiments rely on a subset of the ShapeNet dataset, and we adopt the preprocessing and evaluation workflow introduced by Yang et al. (2019). Each point cloud in the dataset consists of 2048 points sampled on the surface of three shape classes (airplanes, chairs and cars). Objects in the dataset are neither centred with respect to the origin nor scaled uniformly; in fact, the radius of their bounding sphere is normally distributed. We report the *maximum mean discrepancy* (Gretton et al., 2012, MMD) based on the Chamfer Distance (MMD-CD) or the *Earth Mover's Distance* (MMD-EMD) between reconstructed point clouds (see Appendix D for a brief description of these evaluation metrics). Unless otherwise mentioned, the reported Chamfer Distance is scaled by 1.00×10^4 and the Earth Mover's Distance is scaled by 1.00×10^3

> Subsequently, we will refer to the IPT, with the understanding that we are calculating an *approximation* of it according to Eq. (4).

4.1. Reconstructing Point Clouds

Our first set of experiments assesses the reconstruction capabilities of the IP-Encoder. In particular, we investigate (i) the reconstruction quality, (ii) the efficacy of the IPT as a loss, and (iii) the computational efficiency of the IPT. As comparison partners for the reconstruction task we use state-of-the-art models, namely (i) PointFlow (Yang et al., 2019), (ii) SoftFlow (Kim et al., 2020), (iii) ShapeGF (Cai et al., 2020), and (iv) Canonical VAE (Cheng et al., 2022).

Architecture and experimental setup. We consider the IPT as a 1D signal, with each direction corresponding to a channel, sample 256 directions uniformly from the unit sphere, and discretise each direction into 256 steps, thus obtaining an IPT with a resolution of 256×256. The IP-Encoder consists of four 1D convolutional layers with batch normalisation, max-pooling, and ReLU activation functions. After mapping the IPT into an intermediary latent space, we apply a final 3-layer MLP. We use a ReLU activation for the first two layers and a tanh activation for the last layer, as we observe that this works better for the bounded output. Subsequently, we train the IP-Encoder separately for each of the classes for 200 epochs, using a loss term consisting of a weighted sum of the CD and the IPT with a resolution of 64×64. We denote this loss term as CD + IPT-64.

Table 1: Reconstruction results on three ShapeNet classes. The best-performing model is highlighted in **bold**, while the second-best is shown in *italics*. Our method outperforms all comparisons partners in terms of the EMD, which is recognised as the best metric for reconstruction quality (Zhou et al., 2021).

	Airplane		*Chair*		*Car*	
MODEL	CD ($\downarrow$)	EMD ($\downarrow$)	CD ($\downarrow$)	EMD ($\downarrow$)	CD ($\downarrow$)	EMD ($\downarrow$)
PointFlow	1.30 ± 0.00	5.36 ± 0.06	10.43 ± 0.02	17.54 ± 0.16	6.94 ± 0.01	12.93 ± 0.19
SoftFlow	1.19 ± 0.00	4.28 ± 0.06	11.05 ± 0.03	17.68 ± 0.08	6.82 ± 0.01	11.44 ± 0.10
ShapeGF	1.05 ± 0.00	4.42 ± 0.04	**5.96 ± 0.01**	12.23 ± 0.11	*5.68 ± 0.01*	9.26 ± 0.18
Canonical VAE	**0.98 ± 0.00**	*3.19 ± 0.03*	6.56 ± 0.02	*8.60 ± 0.07*	**5.44 ± 0.01**	*6.13 ± 0.02*
IP-Encoder (ours)	*1.03 ± 0.00*	**1.44 ± 0.00**	9.52 ± 0.00	**8.44 ± 0.00**	6.12 ± 0.00	**4.16 ± 0.00**

Results. Our reconstructions (Table 1 and Figure 2a) are of consistently high quality and we outperform all comparison partners in terms of the EMD, which is known to be the most suitable metric to evaluate reconstruction quality (Zhou et al., 2021). Notably, the EMD is *not* used in our loss term. Our method also exhibits substantially reduced training times compared to other methods: The IP-Encoder model requires approximately $25.00\,\mathrm{min}$ on a single GPU, compared to $192.00\,\mathrm{h}$ for PointFlow and more than of $550.00\,\mathrm{h}$ for LION. We additionally perform an ablation study concerning the loss term, showing that the *combination* of CD and IPT is crucial for high reconstruction quality. As Table 2 shows, a joint loss yields the best quality. In line with prior work, CD on its own tends to adversely affect point-cloud density (Achlioptas et al., 2018), resulting in larger (i.e. worse) EMD scores. Conversely, training only with a ECT loss shows that the reconstructed follow the density of the underlying object, but may become blurry. This is partially due to the low resolution of 64, making the combination of CD (for details) and the ECT (for global density and structure) crucial. While it would also possible to use the EMD as a loss term, we find that our IPT-64 loss function is *substantially faster* than the EMD ($0.0006\,\mathrm{s}$ versus $0.0291\,\mathrm{s}$), making it the preferred loss function.

> Our reconstruction experiments demonstrate that the IPT is a highly-efficient and effective representation of point clouds, leading to a conceptually simple model with exceptionally fast training times.

4.2. Generating Novel Point Clouds

Having established that our model is capable of high-quality reconstructions, we now view the IPT as a latent space, from which we can *sample* and subsequently *reconstruct* point clouds using our IP-Encoder model. Subsequently, we demonstrate that (i) the IPT constitutes a highly-stable latent space, (ii) a *distribution* of shapes can be learned through the IPT, and (iii) the IP-Encoder even works well in out-of-sample settings.

Architecture and experimental setup. As a generative model we use a CNN-style VAE (Higgins et al., 2017) model. The encoder of the IP-VAE has four convolutional blocks with Leaky ReLU activation functions, batch normalisation, and a final linear layer for the latent-space embedding. Our latent-space dimension varies depending on the class, with 32, 64 and 150 dimensions for the Car, Airplane and Chair class, respectively. Notably, we consider point cloud generation as a pure image-generation task, meaning that the IP-VAE architecture is fully interchangeable. In addition to the comparison partners used for the reconstruction task, we add three additional generative models, namely (i) SetVAE (Kim et al., 2021), (ii) LION (Zeng et al., 2022), and (iii) Point Voxel Diffusion (Zhou et al., 2021, PVD). All of these models had either only generative capabilities or lacked the code for point-cloud reconstruction, so we excluded them from the prior experiment. For training the IP-VAE, we follow the β-VAE setup, with the KL-divergence as a loss for the latent space, and the MSE as a reconstruction loss. To improve the embedding of IPTs in the latent space, we apply an annealing schedule with $\beta \in [1.00 \times 10^{-8}, 1.00 \times 10^{-4}]$. In the initial 100 epochs, we set β to its maximum value, which emphasises reconstruction, whereas between epochs 100–550, we follow a cosine-based annealing schedule. We sample latent vectors from the IP-VAE and consider them to be IPTs, which we subsequently map to a point cloud using the IP-Encoder model. Our evaluation of generative performance follows (Yang et al., 2019).

Table 2: Ablation study with respect to the loss function. Our joint loss, combining CD and IPT, yields *balanced* results without overfitting any of the two metrics.

	Airplane ($\downarrow$)		*Chair* ($\downarrow$)		*Car* ($\downarrow$)	
LOSS FUNCTION	CD	EMD	CD	EMD	CD	EMD
CD	1.00	8.89	10.44	32.43	5.97	14.96
IPT-64	2.41	1.09	13.06	4.29	7.75	2.47
CD + IPT-64	1.03	1.46	9.52	8.44	6.12	4.16

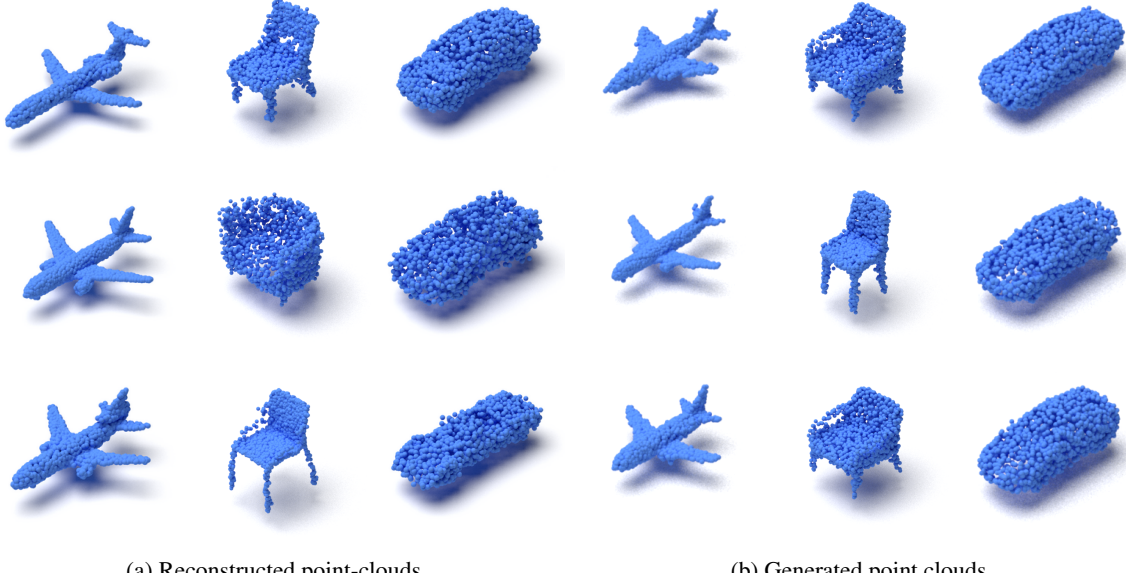(a) Reconstructed point-clouds   (b) Generated point clouds

Figure 2: Examples of *reconstructed* (a) and *generated* (b) point clouds using our IP-Encoder model for three classes in the ShapeNet dataset.

Table 3: Inference time T in s for all methods, measured on the same hardware. Our model is orders of magnitude faster than all others.

MODEL	DEVICE	T (↓)
PointFlow		0.270
SoftFlow		0.120
ShapeGF	GPU	0.340
SetVAE		0.030
PVD		29.900
IP-VAE	GPU	**0.001**
IP-VAE	CPU	**0.006**

Results. Table 4 reports numerical results, while Figure 2b shows generated samples from each class. We include a variety of generative-quality metrics, noting that there is no consensus as to which one is most suitable (Achlioptas et al., 2018; Yang et al., 2019). Despite its conceptual simplicity, our model consistently ranks among the best two models in terms of MMD-EMD, and exhibits performance on a par with more elaborate architectures. This is noteworthy since the IP-VAE is not constrained to produce *exact* IPTs, hence its outputs may contain artefacts. The fact that our IP-Encoder model (which remained fixed throughout this experiment) is able to reconstruct correct point clouds from such out-of-sample data *without* requiring additional regularisation or retraining, demonstrates that the IPT describes a highly-stable and expressive latent space. Moreover, we observe fast training times, with the IP-VAE taking $\approx 10.00\,\mathrm{min}$ to $15.00\,\mathrm{min}$, making the full pipeline run in about $45.00\,\mathrm{min}$. This is in stark contrast to models like LION ($550.00\,\mathrm{h}$) or SoftFlow ($\approx 144.00\,\mathrm{h}$). Finally, as Table 3 shows, our inference times are orders of magnitude faster than existing comparison partners.

> Our generative experiments shows that the IPT is a suitable representation for generating high-quality point clouds, while also exhibiting inference times that are orders of magnitude faster than comparison partners.

4.3. Point-Cloud Upsampling and Compression

Motivated by the promising results in terms of generative performance, we further investigate the capacity of our IP-Encoder model to upsample a downsampled point cloud.

Architecture and experimental setup. We train a downsampling model with the same architecture as the IP-Encoder, resulting in a point cloud with 256 points. In this scenario, the purpose of the loss term is to minimise the discrepancy of the original point cloud to its downsampled version, measured using the IPT, which we normalise because of its dependency on point-cloud cardinality. We then pass the IPT of the downsampled point cloud to the IP-Encoder model to obtain an upsampled version, which, ideally, should be close to the original point cloud. As a comparison partner, we use a uniform-subsampling method, reporting both CD and EMD scores.

Results. Table 5 depicts numerical scores, while Figure 3 depicts example point clouds. Unlike uniform subsampling, our downsampling model preserves uniform density of each object, showing that it has learned the underlying shape. As expected, we observe some loss in quality compared to reconstruction without downsampling, but this is min-

Table 4: Evaluation metrics for point-cloud generation tasks. We highlight the best result in **bold** and the second-best in *italics*. Our implementation of the EMD follows PVD (Zhou et al., 2021), and we report coverage (COV), maximum mean discrepancy (MMD), and 1-NNA for both EMD and CD, respectively.

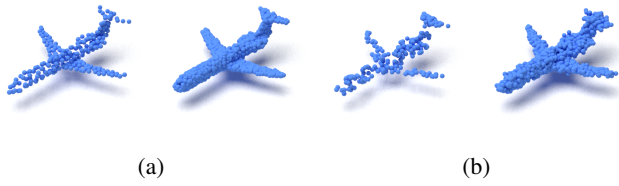|	Airplane						Chair						Car					
	MMD($\downarrow$)		COV($\uparrow$)		1-NNA($\downarrow$)		MMD($\downarrow$)		COV($\uparrow$)		1-NNA($\downarrow$)		MMD($\downarrow$)		COV($\uparrow$)		1-NNA($\downarrow$)	
Model	CD	EMD	CD	EMD	CD	EMD	CD	EMD	CD	EMD	CD	EMD	CD	EMD	CD	EMD	CD	EMD
PointFlow	0.22	0.39	*47.90*	46.41	75.68	69.44	2.41	1.60	42.90	50.00	60.88	59.89	*0.90*	0.81	46.88	50.00	60.65	62.36
SoftFlow	0.23	*0.37*	46.91	47.90	*70.92*	69.44	*2.53*	1.68	41.39	47.43	59.95	63.51	1.19	0.86	42.90	44.60	62.63	64.71
Shape-GF	2.70	0.66	40.74	40.49	80.00	76.17	2.89	1.70	46.67	48.03	68.96	65.48	9.23	0.76	*49.43*	50.28	63.20	56.53
SetVAE	**0.20**	0.37	43.70	48.40	75.31	77.65	2.55	1.59	46.83	44.26	58.76	61.48	**0.88**	**0.73**	49.15	46.59	59.66	61.48
PVD	0.22	0.38	**48.88**	**52.09**	73.82	64.81	2.62	*1.56*	**49.84**	*50.60*	*56.26*	*53.32*	1.08	0.79	41.19	*50.56*	*54.55*	*53.83*
LION	*0.22*	*0.37*	47.16	*49.63*	**67.41**	*61.23*	2.64	**1.55**	*48.94*	**52.11**	**53.70**	**52.34**	0.91	*0.75*	**50.00**	**56.53**	53.41	**51.14**
IP-VAE (Ours)	0.23	**0.32**	46.67	47.65	79.30	**50.00**	**2.50**	**1.55**	37.46	44.11	64.73	64.20	0.96	*0.75*	34.66	49.15	61.79	61.65

(a) (b)

Figure 3: Downsampled (left) and subsequently-upsampled (right) point clouds, using our IP-Downsampler model (a) or uniform subsampling (b).

imal (despite potential compounding errors). Due to the similar setup, we can compare results with Table 1 and we observe that even when downsampling, we *still* perform on a par with the best model in the reconstruction task. Notably, the IP-Encoder has not been retrained for this task, so the IPT of the subsampled point cloud is out-of-distribution. This demonstrates that our model has captured the 'true' underlying shape characteristics.

> Our IP-Encoder can downsample point clouds, yielding high-quality compression with minimal loss of quality.

Table 5: Reconstruction performance for consecutive down- and upsampling, with the best result shown in **bold**. As reference, the last row repeats our reconstruction results (i.e. *without* downsampling).

	Airplane($\downarrow$)		Chair($\downarrow$)		Car($\downarrow$)	
METHOD	CD	EMD	CD	EMD	CD	EMD
IP-Downsampler	**1.18**	**2.58**	**11.70**	**11.42**	**6.42**	**5.81**
Uniform	3.10	4.71	15.38	15.34	9.30	9.09
IP-Encoder	1.03	1.46	9.53	8.45	6.12	4.17

4.4. Inverting IPTs Using Backpropagation

Having focused on the IP-Encoder model, we now briefly discuss how to invert an IPT using backpropagation directly. Our aims are to show that (i) IPTs can be inverted in practice, (ii) a resolution of 128 yields high-quality reconstructions, and (iii) the IPT has *stable gradients* (which is not clear a priori, given that we are approximating an indicator function). Given its differentiability, we can use the IPT directly as a loss term, and use backpropagation to update the coordinates of all point to minimise the overall loss. For this experiment, we train 2000 epochs with the Adam optimizer using a learning rate of 0.5, which we halve in epochs 50, 100, 200, and 1000, respectively. We repeat all experiments with three resolutions and for three choices of scaling factor λ in Eq. (4), which we set either to be equal, half, or a quarter of selected resolution. As a quality metric, we report the EMD and CD between the optimised and target point cloud.

Results. Appendix C and Figure C.3 in the appendix depict the numerical results and show some reconstructed samples, respectively. We observe that all approximations become gradually coarser as the resolution is decreased. Moreover, as expected, we observe problems with vanishing gradients for large values of λ, since the sigmoid function approaches an indicator function in this case. By contrast, for small values of λ, the loss between IPTs reaches zero too quickly, even though the target point cloud has not yet been reached. This requires balancing λ with respect to the resolution, and we empirically observed that around a quarter of the IPT resolution is sufficient for high-quality results, which is how we pick the parameter in practice.

> Backpropagation through IPTs directly is possible but the results are worse than the ones we observe with our IP-Encoder model. Moreover, such an optimisation-based scheme cannot deal with out-of-distribution data.

Figure 4: Linear interpolation between IPTs results in a smooth interpolation in the point-cloud domain. Given the IPT of two airplanes, we linearly interpolate between the pixel values and pass each step through the IP-Encoder to obtain a prediction of the intermediary point cloud. Although the IP-Encoder has not been specifically trained on such data, it is able to produce meaningful reconstructions, since it has learned the distribution of shapes.

4.5. Interpolation in Latent Space

As our final experiment, we consider the linear *interpolation* between the IPT of two point clouds. In the setting of infinite directions, Theorem 2 guarantees that we only encounter valid IPTs along each interpolation. However, in practice, given our use of image-generative models, it is not guaranteed that our input is an IPT in the *strict* sense. Hence, it is crucial to understand the characteristic properties of the IPT in practice since not every sum of sigmoid functions is guaranteed to correspond to a proper shape (in other words, IPTs are not *surjective*). In our discretised representation, interpolating between IPTs can be achieved by interpolating per pixel. To visually assess the quality of the latent space, we reconstruct each intermediary IPT during the interpolation using the IP-Encoder. Figure 4 depicts the resulting point clouds; we observe that the intermediary point clouds still remain plausible reconstructions. Overall, this serves to highlight the utility of the IPT latent space.

> The IPT permits linear interpolations, which in turn result in smooth interpolations between point clouds.

5. Discussion

We propose the *Inner Product Transform* (IPT), which enables us to represent point clouds using 2D images by evaluating inner products. Next to showing that this representation has advantageous theoretical properties, we develop an end-to-end-trainable pipeline for *point-cloud generation*. Notably, we simplify the point-cloud generation process by introducing an intermediate step, the generation of the IPT descriptor, for which one may use *any* image-generation model. Our method is (i) fast (since it uses only inner products and other simple computational building blocks), (ii) well-grounded in theory (it is a sufficient statistic on the space of point clouds), and, (iii) most importantly, we observe that its *reconstruction performance* is the best among all comparison partners, while its *generative capabilities* are at least on a par with more complex models. This is due to the conceptual simplicity of the model and its provably highly-stable latent space, which facilitates performing out-of-distribution tasks *without* the need for retraining or additional regularisation.

Limitations. An unfortunate limitation arising from the disconnect between theory and practice is that our injectivity results only hold for the case of an *infinite* number of directions. Fortunately, set of directions where injectivity fails has measure zero, hence the impact is limited. Deriving additional guidance for selecting parameters like the resolution of the discretised IPT would be helpful. The current formulation of the IPT is also *not* invariant with respect to rotations, which could be a desired property for some applications (or, at the very least, might make the method more robust in the regime of smaller sample sizes). Moreover, if point clouds become high-dimensional, our direction-sampling procedure becomes inefficient—this is not a problem for the shape-generation tasks we are tackling in this paper, though. A larger limitation in point-cloud generation involves the question of evaluation metrics: In the absence of ground-truth information, it is hard to choose the 'best' model (unlike point-cloud reconstruction, where well-defined metrics exist). Even though one could argue that, *ceteris paribus*, computationally efficient models like ours should be preferred in practice, a more in-depth investigation towards improved evaluation metrics seems warranted.

Future work. In a similar vein, future work into more complex model architectures and their capabilities would be intriguing and potentially lead to even better results in terms of quality, albeit at the cost of computational efficiency. We believe *diffusion models* or *transformer-based architectures* to be particularly suitable. Moreover, we hypothesise that the selected directions for computing the IPT would benefit from a proper *positional encoding*, as opposed to our implicit (but simple) encoding. In addition, given the connection of the IPT to more involved geometrical-topological descriptors for graphs, meshes, or higher-order complexes, a natural question is to what extent our inversion results apply to such data; this would help contextualise the IPT within the emerging field of topological deep learning (Papamarkou et al., 2024). A suitable—and feasible—next step would be extension to *graphs*, thus building a bridge between *image generation* and *graph generation*. While we have not yet explored any *single-shot* or even *zero-shot* experiments, we are hopeful that our work (and the IPT as such) may pave the path towards novel *point-cloud foundation models*.

Impact Statement

This paper presents work whose goal is to advance the field of machine learning, specifically the problem of high-quality point-cloud (or shape) generation. Given the computational efficiency of our method, we believe it to be beneficial for 'democratising' access to machine-learning algorithms. There are many other potential societal consequences of point-cloud generation methods, none which we feel must be specifically highlighted here.

References

Achlioptas, P., Diamanti, O., Mitliagkas, I., and Guibas, L. Learning representations and generative models for 3D point clouds. In *International Conference on Machine Learning*, pp. 40–49. PMLR, 2018.

Amézquita, E. J., Quigley, M. Y., Ophelders, T., Landis, J. B., Koenig, D., Munch, E., and Chitwood, D. H. Measuring hidden phenotype: Quantifying the shape of barley seeds using the Euler characteristic transform. *in silico Plants*, 4(1):diab033, 12 2021.

Cai, R., Yang, G., Averbuch-Elor, H., Hao, Z., Belongie, S., Snavely, N., and Hariharan, B. Learning gradient fields for shape generation. In Vedaldi, A., Bischof, H., Brox, T., and Frahm, J.-M. (eds.), *Computer Vision – ECCV 2020*, pp. 364–381, Cham, Switzerland, 2020. Springer.

Cheng, A.-C., Li, X., Liu, S., Sun, M., and Yang, M.-H. Autoregressive 3D shape generation via canonical mapping. In *European Conference on Computer Vision*, pp. 89–104. Springer, 2022.

Crawford, L., Monod, A., Chen, A. X., Mukherjee, S., and Rabadán, R. Predicting clinical outcomes in Glioblastoma: An application of topological and functional data analysis. *Journal of the American Statistical Association*, 115(531):1139–1150, 2020.

Curry, J., Mukherjee, S., and Turner, K. How many directions determine a shape and other sufficiency results for two topological transforms. *Transactions of the American Mathematical Society, Series B*, 9(32):1006–1043, 2022.

Dłotko, P. On the shape that matters–topology and geometry in data science. *European Mathematical Society Magazine*, pp. 5–13, 2024.

Fahim, G., Amin, K., and Zarif, S. Single-view 3D reconstruction: A survey of deep learning methods. *Computers & Graphics*, 94:164–190, 2021. doi: 10.1016/j.cag.2020.12.004.

Fasy, B. T., Micka, S., Millman, D. L., Schenfisch, A., and Williams, L. Challenges in reconstructing shapes from Euler characteristic curves, 2018. URL https://arxiv.org/abs/1811.11337.

Ghrist, R., Levanger, R., and Mai, H. Persistent homology and Euler integral transforms. *Journal of Applied and Computational Topology*, 2(1):55–60, 2018.

Gretton, A., Borgwardt, K. M., Rasch, M. J., Schölkopf, B., and Smola, A. A kernel two-sample test. *Journal of Machine Learning Research*, 13(25):723–773, 2012.

Higgins, I., Matthey, L., Pal, A., Burgess, C., Glorot, X., Botvinick, M., Mohamed, S., and Lerchner, A. β-VAE: Learning basic visual concepts with a constrained variational framework. In *International Conference on Learning Representations*, 2017.

Kim, H., Lee, H., Kang, W. H., Lee, J. Y., and Kim, N. S. SoftFlow: Probabilistic framework for normalizing flow on manifolds. In Larochelle, H., Ranzato, M., Hadsell, R., Balcan, M., and Lin, H. (eds.), *Advances in Neural Information Processing Systems*, volume 33, pp. 16388–16397. Curran Associates, Inc., 2020.

Kim, J., Yoo, J., Lee, J., and Hong, S. SetVAE: Learning hierarchical composition for generative modeling of set-structured data. In *Proceedings of the IEEE/CVF Conference on Computer Vision and Pattern Recognition (CVPR)*, pp. 15059–15068, 2021.

Liu, Z., Tang, H., Lin, Y., and Han, S. Point-Voxel CNN for efficient 3D deep learning. In Wallach, H., Larochelle, H., Beygelzimer, A., d'Alché-Buc, F., Fox, E., and Garnett, R. (eds.), *Advances in Neural Information Processing Systems*, volume 32. Curran Associates, Inc., 2019.

Marsh, L., Zhou, F. Y., Qin, X., Lu, X., Byrne, H. M., and Harrington, H. A. Detecting temporal shape changes with the Euler characteristic transform. *Transactions of Mathematics and Its Applications*, 8, 2024.

Mémoli, F. and Sapiro, G. Comparing point clouds. In *Proceedings of the 2004 Eurographics/ACM SIGGRAPH Symposium on Geometry Processing*, pp. 32–40, 2004.

Munch, E. An invitation to the Euler characteristic transform, 2023. URL https://arxiv.org/abs/2310.10395.

Nadimpalli, K. V., Chattopadhyay, A., and Rieck, B. Euler characteristic transform based topological loss for reconstructing 3D images from single 2D slices. In *Proceedings of the IEEE/CVF Conference on Computer Vision and Pattern Recognition Workshops (CVPRW)*, pp. 571–579, 2023.

Papamarkou, T., Birdal, T., Bronstein, M., Carlsson, G., Curry, J., Gao, Y., Hajij, M., Kwitt, R., Liò, P., Lorenzo,

P. D., Maroulas, V., Miolane, N., Nasrin, F., Ramamurthy, K. N., Rieck, B., Scardapane, S., Schaub, M. T., Veličković, P., Wang, B., Wang, Y., Wei, G.-W., and Zamzmi, G. Position: Topological deep learning is the new frontier for relational learning. (235):39529–39555, 2024.

Qi, C. R., Yi, L., Su, H., and Guibas, L. J. PointNet++: Deep hierarchical feature learning on point sets in a metric space. In Guyon, I., Luxburg, U. V., Bengio, S., Wallach, H., Fergus, R., Vishwanathan, S., and Garnett, R. (eds.), *Advances in Neural Information Processing Systems*, volume 30. Curran Associates, Inc., 2017.

Röell, E. and Rieck, B. Differentiable Euler characteristic transforms for shape classification. In *International Conference on Learning Representations*, 2024.

Tancik, M., Srinivasan, P., Mildenhall, B., Fridovich-Keil, S., Raghavan, N., Singhal, U., Ramamoorthi, R., Barron, J., and Ng, R. Fourier features let networks learn high frequency functions in low dimensional domains. In Larochelle, H., Ranzato, M., Hadsell, R., Balcan, M., and Lin, H. (eds.), *Advances in Neural Information Processing Systems*, volume 33, pp. 7537–7547. Curran Associates, Inc., 2020.

Turner, K., Mukherjee, S., and Boyer, D. M. Persistent homology transform for modeling shapes and surfaces. *Information and Inference: A Journal of the IMA*, 3(4): 310–344, 12 2014.

Xu, Q.-C., Mu, T.-J., and Yang, Y.-L. A survey of deep learning-based 3D shape generation. *Computational Visual Media*, 9(3):407–442, 2023. doi: 10.1007/s41095-022-0321-5.

Yang, G., Huang, X., Hao, Z., Liu, M.-Y., Belongie, S., and Hariharan, B. PointFlow: 3D point cloud generation with continuous normalizing flows. In *IEEE/CVF International Conference on Computer Vision (ICCV)*, pp. 4540–4549, 2019. doi: 10.1109/ICCV.2019.00464.

Zaheer, M., Kottur, S., Ravanbakhsh, S., Poczos, B., Salakhutdinov, R. R., and Smola, A. J. Deep sets. In Guyon, I., Luxburg, U. V., Bengio, S., Wallach, H., Fergus, R., Vishwanathan, S., and Garnett, R. (eds.), *Advances in Neural Information Processing Systems*, volume 30. Curran Associates, Inc., 2017.

Zeng, X., Vahdat, A., Williams, F., Gojcic, Z., Litany, O., Fidler, S., and Kreis, K. LION: Latent point diffusion models for 3D shape generation. In Koyejo, S., Mohamed, S., Agarwal, A., Belgrave, D., Cho, K., and Oh, A. (eds.), *Advances in Neural Information Processing Systems*, volume 35, pp. 10021–10039. Curran Associates, Inc., 2022.

Zhou, L., Du, Y., and Wu, J. 3D shape generation and completion through Point-Voxel Diffusion. In *Proceedings of the IEEE/CVF International Conference on Computer Vision (ICCV)*, pp. 5826–5835, October 2021.
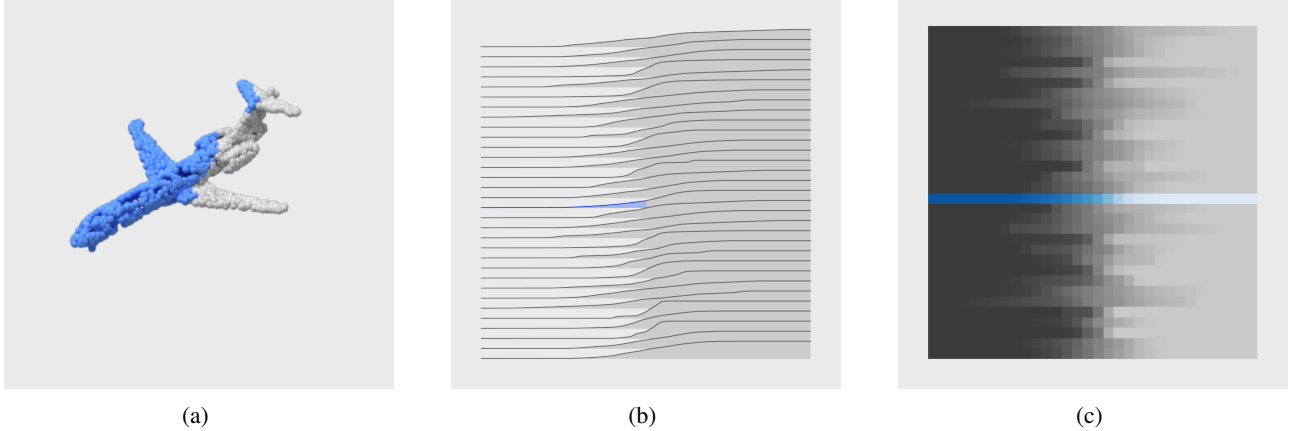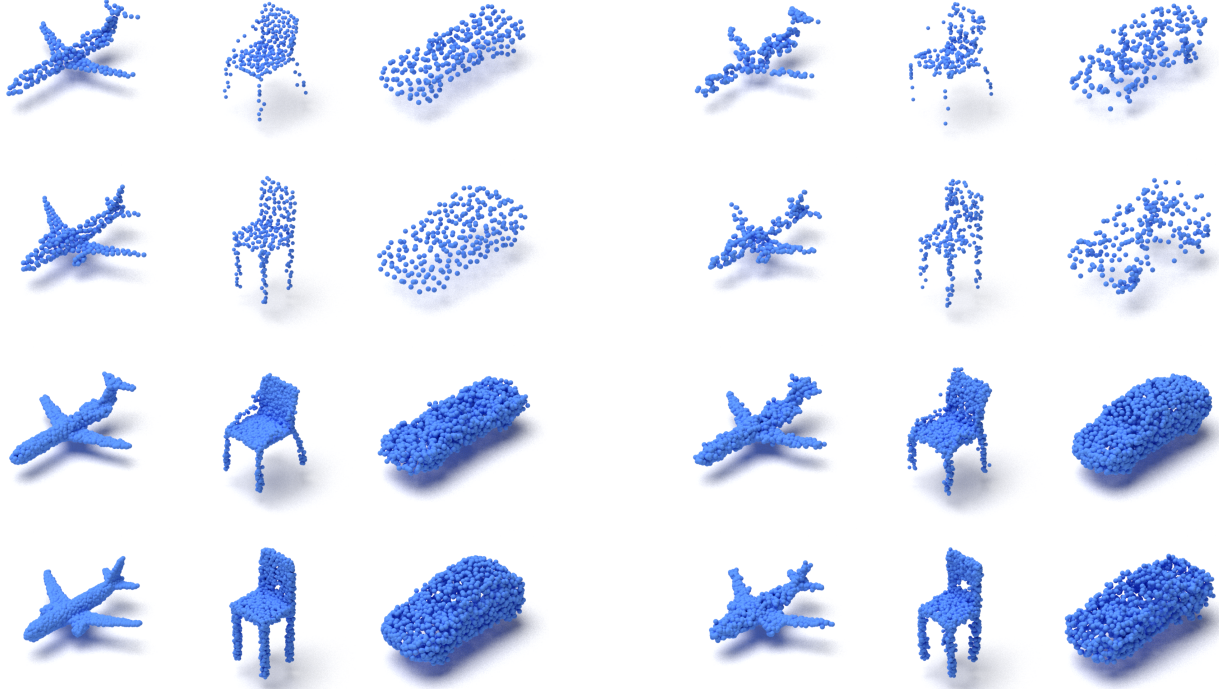
A. Overview of the IPT

| (a) | (b) | (c) |

Figure A.1: An overview of the IPT calculation for 32 directions and resolution of 32. For a given direction vector ξ, we filter the point cloud with hyperplanes. The partially filtered point cloud is shown in (a) and points included in the filtration are colored blue. For each of the 32 directions, sampled uniformly from the sphere, the respective curves along each direction are shown in (b) and the partially-completed curve from (a) is highlighted. Note that neighbouring curves are *not* necessarily related, requiring us to treat each curve as its own signal. Each of the 32 curves is discretised in 32 steps and stacked to form an *image* representation of the point cloud (c) of size 32×32. The row corresponding to the full curve from (a) and each of the rows corresponds to the curve in the same index in (b). For complex geometries such as the ShapeNet data, we empirically observe that at least 128 directions are required, using a resolution of 128.

B. Additional Downsampling Figures

We provide a more extensive version of Figure 3 for the comparison of downsampling with the IP-Downsampler (left) and uniform subsampling (right) for all three classes.

(a) Downsampled point-clouds with the IP-Downsampler (top) and upsampled with the IP-Encoder (bottom).

(b) Downsampled point clouds with uniform subsampling (top) and upsampled with the IP-Encoder (bottom).

Figure B.2: A visual comparison between down- and upsampling using our IP-Downsampler (a) and uniform subsampling (b). The downsampled point clouds using the IP-Downsampler are equidistantly spread, in contrast to uniform subsampling. Higher upsampling quality follows, compared to uniform subsampling. Our model has a bias towards equidistant point clouds and leads to a better representation of the underlying shape.

C. Additional Experiments

Table C.1: Reconstruction results for rendering of the three ShapeNet classes. A point cloud is randomly initialized and optimized with the IPT as a loss function. The experiment is repeated for different resolutions and for different scales. The ideal scale is $1/4$ of the resolution, corresponding to the bottom row.

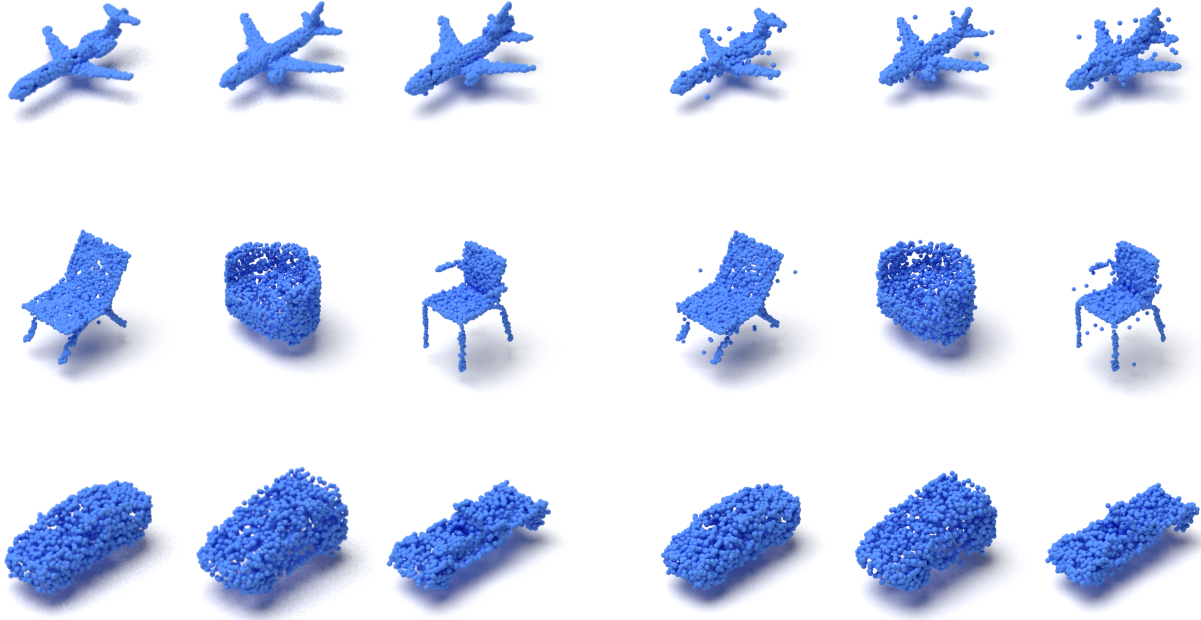| RESOLUTION	SCALE FACTOR	Airplane		Car		Chair	
		CD ($\downarrow$)	EMD ($\downarrow$)	CD ($\downarrow$)	EMD ($\downarrow$)	CD ($\downarrow$)	EMD ($\downarrow$)
	128	1.27 ± 0.00	0.29 ± 0.00	2.97 ± 0.00	0.55 ± 0.00	3.40 ± 0.01	0.65 ± 0.00
128	64	0.75 ± 0.00	0.18 ± 0.00	2.15 ± 0.00	0.42 ± 0.00	2.10 ± 0.00	0.41 ± 0.00
	32	0.52 ± 0.00	0.12 ± 0.00	2.04 ± 0.00	0.39 ± 0.00	1.83 ± 0.00	0.35 ± 0.00
	64	2.65 ± 0.01	0.57 ± 0.00	4.76 ± 0.01	0.85 ± 0.00	5.83 ± 0.01	1.10 ± 0.00
64	32	1.88 ± 0.01	0.40 ± 0.00	4.05 ± 0.01	0.70 ± 0.00	4.29 ± 0.00	0.78 ± 0.00
	16	1.22 ± 0.00	0.26 ± 0.00	3.80 ± 0.00	0.64 ± 0.00	3.62 ± 0.00	0.62 ± 0.00
	32	6.21 ± 0.01	1.32 ± 0.00	9.85 ± 0.01	1.99 ± 0.00	16.92 ± 0.02	3.54 ± 0.01
32	16	4.11 ± 0.01	0.90 ± 0.00	8.56 ± 0.02	1.63 ± 0.00	12.55 ± 0.02	2.53 ± 0.00
	8	2.77 ± 0.00	0.61 ± 0.00	7.24 ± 0.01	1.35 ± 0.00	9.05 ± 0.00	1.73 ± 0.00

Figure C.3: Examples of *rendered* point clouds using our optimisation scheme for the three classes of ShapeNet. On the left, the point clouds are rendered at a resolution of 128 with a scale of 32, leading to high quality reconstructions. The right shows the same rendering with the scale set to 128, where the gradients are unstable. The resulting rendered point clouds have only partially converged, with some clear outliers.

D. Metrics for Point Clouds

A good metric for point-cloud generation balances computational speed and theoretical guarantees. Finding such metrics is a challenging task, since often computations require the consideration of all pairs of points between the two point clouds. An example is the Gromov-Hausdorff distance (Mémoli & Sapiro, 2004), which has advantageous theoretical properties, but is hard to evaluate. Two metrics are commonly used to describe the distance between point clouds, the Chamfer Distance (CD) and Earth Movers Distance (EMD), to which we present a self-contained summary here. Although not a metric in the mathematical sense, the Chamfer Distance (CD) poses a good balance between computational speed and quality and is defined for point clouds X and Y as

$$\text{CD}(X, Y) = \sum_{x \in X} \min_{y \in Y} \|x - y\| + \sum_{y \in Y} \min_{x \in X} \|x - y\|. \tag{8}$$
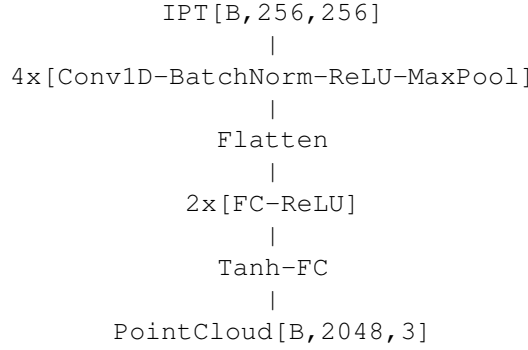
Another commonly used metric is the Earth Movers Distance (EMD). The distance between point clouds is viewed as the cost required to transport one point-cloud into the other and is defined as

$$\text{EMD}(X, Y) = \min_{\phi:X \to Y} \sum_{x \in X} \|x - \phi(x)\|, \tag{9}$$

where ϕ solves an optimal transport problem. Solving the optimal transport problem is a computationally intensive task that becomes prohibitive for medium to large point clouds. The properties of using the CD as loss term were investigated in Achlioptas et al. (2018) and revealed that reconstructions had non-uniform surface density, compared to the uniformly sampled ground truth points. A strong advantage of the CD is the computational efficiency for medium to large point-cloud sizes.
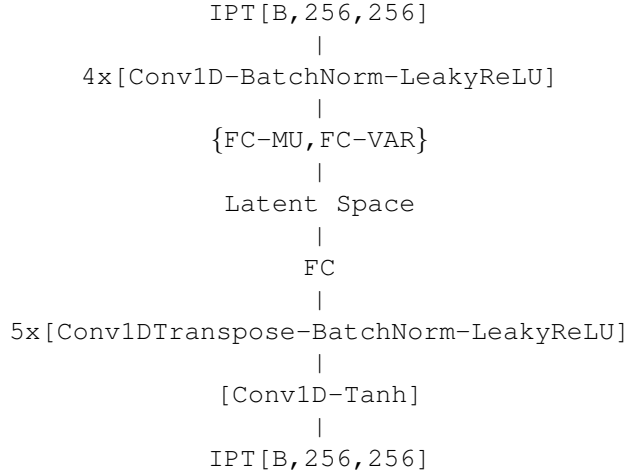
E. Architectural Details

We provide the details of both the IP-Encoder and IP-VAE architecture. The IPT as defined in Eq. (4) is viewed as an image of shape $n_h \times n_d$, where n_h is the discretisation of the heights along each direction and n_d is the number of directions. In the architecture, n_d will be channels in the CNN and to accommodate for that we expect the input to be of the form $n_b \times n_d \times n_h$, where n_b is the batch size. In all our experiments we set $n_d = n_h = 256$ and denote a batch of IPTs in the diagram with `IPT[B,256,256]`. The internal architecture of the IP-Encoder is:

```
               IPT[B,256,256]
                     |
    4x[Conv1D-BatchNorm-ReLU-MaxPool]
                     |
                  Flatten
                     |
               2x[FC-ReLU]
                     |
                  Tanh-FC
                     |
           PointCloud[B,2048,3]
```

Here, `PointCloud[B,2048,3]` denotes the *final* predicted batch of point clouds.

Our IP-VAE has the following architecture:

```
               IPT[B,256,256]
                     |
      4x[Conv1D-BatchNorm-LeakyReLU]
                     |
              {FC-MU,FC-VAR}
                     |
               Latent Space
                     |
                     FC
                     |
   5x[Conv1DTranspose-BatchNorm-LeakyReLU]
                     |
              [Conv1D-Tanh]
                     |
               IPT[B,256,256]
```

In the diagram above, latent embeddings are denoted by `FC-MU` and `FC-VAR`, respectively.

F. Properties of the Inner Product Transform

This section discusses all proofs for statements from the main paper. While the first result about the injectivity is already known, we provide a novel, highly-accessible proof, which only requires basic concepts from linear algebra.

Theorem 1. *The IPT is* injective*, i.e.* $X \neq Y$ *implies that* $\mathrm{IPT}(X) \neq \mathrm{IPT}(Y)$ *for two point clouds* X, Y.

Two point-clouds $X, Y \subset \mathbb{R}^n$ are considered equal if they have the same cardinality and they are equal in the sense of sets. To prove injectivity of the Inner Product Transform, we need to show that for any two point-clouds with $X \neq Y$, we have $\mathrm{IPT}(X) \neq \mathrm{IPT}(Y)$.

Proof. Let $X, Y \subset \mathbb{R}^n$ with $X \neq Y$ and let Ξ be a set of $n + 1$ linearly independent directions. Given $\xi \in \Xi$, write $X_\xi := \{x \cdot \xi \mid x \in X\}$ for the projection of X onto the one-dimensional subspace along ξ. Here, $\xi \cdot x$ denotes the usual Euclidean inner product. If for any direction $\xi \in \Xi$ we have $X_\xi \neq Y_\xi$, we are done because this means that there are $\xi_1 < \xi_2 \in \Xi$ such that the cardinality of X changes but the cardinality of Y does not change or vice versa. Thus, let us assume that $X_\xi = Y_\xi$ for all directions ξ. For each ξ, we may thus sort the values by magnitude and calculate differences, i.e. expressions of the form $x \cdot w - y \cdot w$. Assume that for all ξ, the elements of X_ξ are unique. The set of directions that do not satisfy this condition has measure zero in S^{n-1}. Now we know that $x \cdot \xi - y \cdot \xi = 0$ by assumption and we may rewrite this as $(x - y) \cdot \xi = 0$ for all directions $\xi \in \Xi$. Treating this as a system of $n + 1$ linear equations, this is tantamount of writing that the kernel of the corresponding linear map is the *full column space*. The latter part follows because the directions are chosen linearly independently and because $|\Xi| \geq n + 1$. Thus, the linear system has rank 0 so all coefficients must be zero, implying that the point clouds are the same. This is a contradiction, so our initial assumption must have been wrong. Thus, there is $\xi \in \Xi$ such that $X_\xi \neq Y_\xi$, implying that $\mathrm{IPT}(X) \neq \mathrm{IPT}(Y)$. $\square$

Lemma 1. *Let $B_n(R)$ denote a ball of radius R in $\mathbb{R}^n$. For two point clouds $X, Y \in B_n(R)$, define their* distance *as*

$$d(X, Y) := \frac{1}{|\Xi|} \sum_{\xi \in \Xi} \|\mathrm{IPT}(X)_{\restriction \xi} - \mathrm{IPT}(Y)_{\restriction \xi}\|_2, \tag{5}$$

where Ξ is a finite set of directions and $\| \cdot \|_2$ is the L^2-norm restricted to the interval $[-R, R]$. The function $d(\cdot, \cdot)$ satisfies the definition of a metric.

Proof. If $d(X, Y) = 0$ then $\|\mathrm{IPT}(X) - \mathrm{IPT}(Y)\|_2 = 0$ and since $\| \cdot \|_2$ is a metric, it follows that $\mathrm{IPT}(X) = \mathrm{IPT}(Y)$. Since the IPT is injective, we conclude that $X = Y$. Equality in this case is seen as equality the of sets, that is up to permutation. Both the reverse implication and symmetry follow from the definitions. For the triangle inequality we verify

$$\begin{aligned} d(X, Y) &= \|\mathrm{IPT}(X) - \mathrm{IPT}(Y)\|_2 \\ &= \|(\mathrm{IPT}(X) - \mathrm{IPT}(Z)) - (\mathrm{IPT}(Y) - \mathrm{IPT}(Z))\|_2 \\ &\leq \|\mathrm{IPT}(X) - \mathrm{IPT}(Z)\| + \|\mathrm{IPT}(Y) - \mathrm{IPT}(Z)\|_2 \\ &= d(X, Z) + d(Z, Y). \end{aligned} \tag{10}$$

$\square$

Lemma 2. *Let $X, Y \subset \mathbb{R}^n$ be disjoint point clouds, then*

$$\mathrm{IPT}(X \cup Y) = \mathrm{IPT}(X) + \mathrm{IPT}(Y). \tag{6}$$

Proof. It follows from the definition of the IPT that for all $\xi \in S^{n-1}$ and $h \in \mathbb{R}$ we have

$$\begin{aligned} \mathrm{IPT}(X \cup Y) &= \sum_{x \in X \cup Y} \mathbb{1}_x(\xi, h) \\ &= \sum_{x \in X} \mathbb{1}_x(\xi, h) + \sum_{y \in Y} \mathbb{1}_y(\xi, h) \\ &= \mathrm{IPT}(X) + \mathrm{IPT}(Y). \end{aligned} \tag{11}$$

The second equality uses that the intersection of X and Y is empty, implying that a point is either in X or in Y. $\square$

Theorem 2. *Given two point clouds $X, Y \subset \mathbb{R}^n$. The IPT is* surjective *for the rational linear subspace spanned by* $\mathrm{IPT}(X)$ *and* $\mathrm{IPT}(Y)$*, up to a rational scaling factor. In particular, for $p, q \in \mathbb{N}_0$ with $0 \leq p \leq q$ we have*

$$\frac{p}{q}\mathrm{IPT}(X) + \frac{q-p}{q}\mathrm{IPT}(Y) = \frac{1}{q}\mathrm{IPT}(Z), \tag{7}$$

where $Z = \cup_p X \cup_{q-p} Y$.

Proof. To show surjectivity it suffices to show that for any rational linear combination of IPTs there exists a point cloud $Z \subset \mathbb{R}^n$ that has an IPT equal to that linear combination, up to a rational coefficient. This is to say that $\forall \alpha, \beta \in \mathbb{Q} \exists \gamma \in \mathbb{Q}$ such that

$$\alpha\mathrm{IPT}(X) + \beta\mathrm{IPT}(Y) = \gamma\mathrm{IPT}(Z). \tag{12}$$

Let $\alpha = p/q$ and $\beta = r/s$, then

$$qs\left[\frac{p}{q}\mathrm{IPT}(X) + \frac{r}{s}\mathrm{IPT}(Y)\right] = sp\mathrm{IPT}(X) + qr\mathrm{IPT}(Y)$$
$$= \mathrm{IPT}(\cup_{sp} X \cup_{qr} Y). \tag{13}$$

Thus, setting $\gamma = 1/qs$ and $Z = \cup_{sp} X \cup_{qr} Y$ does the trick. We conclude that the IPT is surjective on rational linear combinations. Let $0 \leq p \leq q$, statement follows from the equalities

$$\frac{p}{q}\mathrm{IPT}(X) + \frac{q-p}{q}\mathrm{IPT}(Y)$$
$$= \frac{1}{q}\left[p\,\mathrm{IPT}(X) + (q-p)\,\mathrm{IPT}(Y)\right]$$
$$= \frac{1}{q}\left[\mathrm{IPT}\left(\cup_p X\right) + \mathrm{IPT}\left(\cup_{q-p} Y\right)\right]$$
$$= \frac{1}{q}\mathrm{IPT}\left(\cup_p X \cup_{q-p} Y\right). \tag{14}$$

$\square$